INTERNATIONAL JOURNAL FOR NUMERICAL METHODS IN FLUIDS
Int. J. Numer. Meth. Fluids 2009; **60**:1222–1240
Published online 20 October 2008 in Wiley InterScience (www.interscience.wiley.com). DOI: 10.1002/fld.1930

Drag reduction by flow separation control on a car after body

Mathieu Rouméas[1], Patrick Gilliéron[1] and Azeddine Kourta[2,*,†]

[1]*Groupe 'Mécanique des Fluides et Aérodynamique', Direction de la recherche Renault, 1, avenue du Golf (TCR AVA 058), 78288 Guyancourt, France*
[2]*Institut de Mécanique des Fluides de Toulouse, Groupe EMT2 Avenue du professeur Camille Soula, 31000 Toulouse, France*

SUMMARY

New development constraints prompted by new pollutant emissions and fuel consumption standards (Corporate Average Economy Fuel) require that automobile manufacturers develop new flow control devices capable of reducing the aerodynamic drag of motor vehicles. The solutions envisaged must have a negligible impact on the vehicle geometry. In this context, flow control by continuous suction is seen as a promising alternative. The control configurations identified during a previous 2D numerical analysis are adapted for this purpose and are tested on a 3D geometry. A local suction system located on the upper part of the rear window is capable of eliminating the rear window separation on simplified fastback car geometry. Aerodynamic drag reductions close to 17% have been obtained. Copyright © 2008 John Wiley & Sons, Ltd.

Received 7 September 2007; Revised 19 August 2008; Accepted 21 August 2008

KEY WORDS: lattice Boltzmann method; separation; longitudinal vortices; drag reduction; active control; suction

INTRODUCTION

New constraints in terms of pollutant emissions and fuel consumption (Corporate Average Economy Fuel) are warranting the development of new flow control devices capable of reducing the aerodynamic drag of motor vehicles. In this context, the objective is to modify the near wall flow and thereby limit the development and dissipation of the separated vortices that contribute towards the development of aerodynamic drag.

The optimization of vehicle shapes and the incorporation of commonly used passive control devices have already brought about a significant aerodynamic drag reduction (from $C_x = 0.45$ in 1975 to $C_x = 0.35$ in 1985 [1, 2], C_x being the average drag coefficient). The need to further reduce

*Correspondence to: Azeddine Kourta, Institut de Mécanique des Fluides de Toulouse, Groupe EMT2 Avenue du professeur Camille Soula, 31000 Toulouse, France.
†E-mail: kourta@imft.fr

fuel consumption and/or provide automobile designers with more creative liberty is prompting the automobile industry to develop innovative active flow control solutions. Such solutions [2] use an external energy source to modify the flow topology without necessarily modifying the shape of the vehicle. Flow control was extensively studied and applied [3, 4] and control theory was developed [5, 6]. Different control techniques have been analysed in university and industrial laboratories and significant results have been obtained on academic geometries [2]. Continuous suction and/or blowing solutions offer a promising alternative [7, 8] and seem well-adapted to the automobile context [9]. For example, the efficiency of a suction system in controlling the separation of the boundary layer has been highlighted experimentally on a cylinder by Bourgois and Tensi [10] and Fournier *et al.* [11]. The results indicate that significant drag reductions, close to 30%, are obtained by moving the flow separation downstream; similar results are obtained by Rouméas *et al.* [12] on a simplified 2D fastback car geometry. In this case, the drag reduction is associated with the elimination of the separated layer on the rear window when suction is applied.

Such control solutions, however, cannot be installed on a real vehicle until further investigations have been carried out. In particular, the results obtained in a 2D configuration [12] must be tested on a 3D numerical model in order to represent the longitudinal vortices that appear on the lateral edges of the rear window and contribute significantly to the development of aerodynamic drag [13–17].

A 3D numerical simulation is, therefore, implemented to analyse the influence of suction on the flow topology developing around simplified fastback car geometry [17]. The flow topology obtained without control and the numerical method, based on the lattice Boltzmann method (LBM), is detailed in a previous publication [17, 18].

In the first part, a numerical method and parameters are detailed. A simplified integral formulation of the aerodynamic drag [13] is presented in the second part to specify the control objectives. The flow topology obtained with suction is analysed in the third part to identify the influence of suction mainly to prevent separation and secondary on the longitudinal vortices development. Finally, the aerodynamic drag values obtained with and without control are compared at different suction velocities to determine the efficiency of the flow control devices.

NUMERICAL METHOD

The numerical method used in a previous paper [17] is applied here. It consists of a 3D numerical simulation based on Powerflow code with an LBM. This method is based on microscopic models and mesoscopic kinetic equations. The fundamental principle of the LBM is to construct simplified kinetic models that incorporate the essential physics of microscopic or mesoscopic processes such that the macroscopic-averaged properties conform to the desired macroscopic equations. The basic premise for using these simplified kinetic-type methods for macroscopic fluid flows is that the macroscopic fluid dynamics are the result of the collective behaviour of many microscopic particles in the system and that the macroscopic dynamics are not sensitive to the underlying details as is the case in microscopic physics [17, 18].

The fluid particles are distributed on a Cartesian lattice of computation nodes [13]. For each lattice node, a distribution function $[f_i]_{i=1\ldots N}$ is associated with a discrete velocity distribution $[\mathbf{V}_i]_{i=1\ldots N}$ representing N possible velocities of motion. The kinetic energy is given by $\bar{e}=\frac{1}{2}\sum_{i=1}^{N} V_i^2$. One particle placed on one node may stay at this node (energy level $0:\bar{e}=0$), move towards an adjacent node in horizontal or vertical plane (energy level $1:\bar{e}=1$) or move to a farthest node (energy level $2:\bar{e}=2$). The model gives 34 possible combinations and is called 34 velocities model

DOI: 10.1002/fld

(2 possibilities for level 0, 18 for level 1 and 14 for level 2). More details concerning the algorithm can be found in [17–21].

The general algorithm for the LBM is thus defined in four stages. The first consists in propagating the distribution function in time $t+1$ [22, 23]. In the second stage, the collisions between the particles are modelled. The collision operator is then applied to time $t-1$. The third stage consists in determining the associated values of density and momentum. Finally, the fourth stage consists in initiating iteration on the basis of the macroscopic values determined in the third stage.

As in the case of all numerical space–time discretization methods, the LBM is not capable of resolving all turbulence scales. The computation code, therefore, uses a turbulence model, which introduces a turbulent viscosity into the initial model. The turbulence model is the RNG k–ε model originally developed by Yakhot and Orszag [24]. The equations describing the transport of kinetic energy and dissipation applied by the model are resolved on the same lattice as the Boltzmann equations. The discretization diagram used is a second order in space (Lax–Wendroff finite difference model) associated with a time-explicit integration diagram [25]. Close to the wall, a specific velocity law is applied to limit the computational workload [25]. The velocity is then described by a logarithmic law.

The numerical simulations presented in this paper were conducted on a simplified vehicle geometry initially proposed by Ahmed *et al.* [14]. The computation is exclusively focused on the rear part. The geometry is the same as the one previously computed without control [17].

The geometry is defined by its length ($L=1.044\,\mathrm{m}$), its width ($l=0.389\,\mathrm{m}$) and its height ($H=0.288\,\mathrm{m}$). In this configuration, the rear window with a length of $0.222\,\mathrm{m}$ is inclined at an angle of 25° with respect to the horizontal. Finally, the lower part is positioned at $h=0.17H$ from the floor of the numerical wind tunnel. The geometry is located in a rectangular numerical section of length, width and height equal to $31L$, $20l$ and $10H$, respectively. These dimensions ensure that there is no interaction between the boundary conditions imposed at the limit of the computational domain and the development of the near-wake flow, as has been demonstrated in [17]. The outlet condition, downstream from the geometry and on the upper part, is a free flow condition [17] on pressure and velocity. The flow is advected from left to right and a uniform velocity $V_0=40\,\mathrm{m\,s^{-1}}$ is applied to the left-hand surface of the simulation domain (Dirichlet velocity condition). The Reynolds number associated with length L of the geometry is $Re=2.8\times10^6$. Finally, symmetry conditions are applied on the side surfaces of the simulation domain [17].

SUMMARY OF THE PERVIOUS RESULTS OBTAINED WITHOUT CONTROL

In previous paper [17], results obtained without control in this geometry have been compared with previous computational and experimental results. The longitudinal velocity profiles in the vertical direction (Figure 6 of this reference), measured on the median longitudinal plane, were compared with the experimental data at six positions: the end of the roof, the top of the rear window, the first part of the rear window, the middle of the rear window, the last part of the rear window and at the bottom of the rear window. It has been concluded that the computation code is able to predict both the separation and attachment of the fluid, respectively, on the top and bottom of the rear window. This aspect, a common problem in the numerical representation of the flow around fastback geometry, is correctly processed by the code. However, the computation code overestimates the velocity defect in the boundary layer, close to the re-attachment. The results obtained in the separated boundary layer are associated with the logarithmic law used to define

DOI: 10.1002/fld

the velocity evolution close to the wall. As known, this law is not adapted to the separated region. The accuracy of these results has been evaluated by determining the differences with experimental results considered as a basis of comparison. In the external region the error is less than 1%, but it can reach 11–13% in the separation zone where the computation is less accurate. In addition, in the same paper [17], the friction line traces on the rear window (Figure 7 of this reference), indicate that the computation code correctly represents the physical phenomena highlighted in the experiments. Finally, drag coefficient has been compared with previous experimental and numerical (RANS [26], LES [27, 28]) studies. Good agreement has been obtained both with experiment and LES computation.

In the present paper, for the same geometry and with the same numerical conditions, the control is applied and obtained results will be compared with the previous case without control.

THEORETICAL BASES

Aerodynamic drag is defined as an integral over the surface vehicle of the static pressure, friction and turbulence stresses. The obtained equation constitutes an overall expression of the aerodynamic drag without highlighting the contribution of the various separated vortices. To obtain a better understanding of various physical phenomena (and their mutual interaction), it is necessary to develop simplified approaches conducive to identifying which parameters play a significant role in achieving a reduction in aerodynamic drag. Onorato *et al.* [13] propose a simplified analytical model based on the momentum equation applied to the air inside a stream tube enclosing the vehicle (see Figure 1). The flow is assumed to be steady, incompressible, and gravity and turbulence effects are considered negligible compared with the pressure effect [7]. These simplifications lead to the Onorato expression of the aerodynamic drag:

$$F_x = -\frac{\rho V_0^2}{2}\int_S \left(1-\frac{V_x}{V_0}\right)^2 \mathrm{d}\sigma + \frac{\rho V_0^2}{2}\int_S \left(\frac{V_y^2}{V_0^2}+\frac{V_z^2}{V_0^2}\right)\mathrm{d}\sigma + \int_S (P_{i0}-P_i)\,\mathrm{d}\sigma \tag{1}$$

where P_{i0} is the reference total pressure, V_0 the external flow velocity, ρ the density, P_i the total pressure and V_x, V_y, V_z the components of the velocity vector. The Onorato expression (1) is then used to define the aerodynamic drag of a motor vehicle according to velocity and total pressure fields measured in the wake cross section S, downstream from the base.

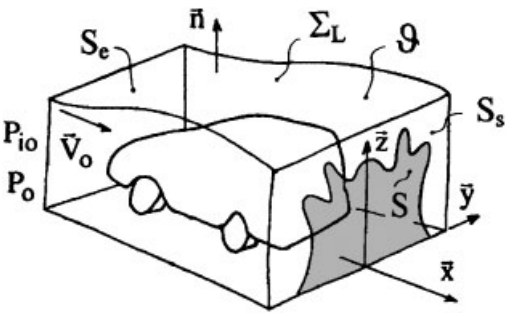

Figure 1. Schematic of the stream tube used for the Onorato expression, Gilliéron [9].

DOI: 10.1002/fld

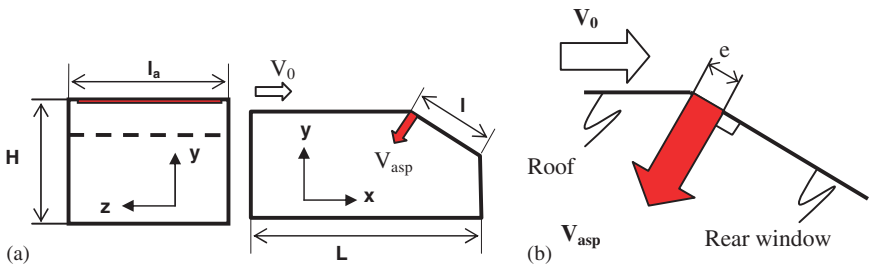

Figure 2. Schematic of the used geometry and implementation of the control system.

The first term of the expression (1) represents the drag associated with the longitudinal velocity deficit measured inside the near-wake zone. It is associated with the development of transversal vortices at the base [14]. The second term corresponds to the vortex drag, associated with the development of longitudinal vortices on the geometry. Finally, the third term expresses the drag induced by the total pressure loss between the upstream and the downstream of the motor vehicle, associated with the formation and maintenance of separated swirling structures in the wake.

According to the Onorato expression (1), the aerodynamic drag of a motor vehicle is mainly due to the formation of separated flow on the geometry, and the formation of transversal and longitudinal swirling structures in the wake. Therefore, the drag reduction can be obtained by reducing, or even eliminating, the longitudinal vortices (second term), by reducing the wake cross section S or by limiting the total pressure loss in the wake (third term).

In this study, the objective is to move downstream, or even to eliminate, the flow separation on the rear window in such a way as to reduce the wake cross section and the associated volume energy loss. According to a previous 2D numerical study [12], the control consists of a continuous suction located on the rear window. The computation code used is based on the LBM and an RNG k–ε schema provides a model of the turbulence effects. The numerical protocol used, in particular with respect to the mesh, is detailed by Rouméas *et al.* [17].

The suction system consists of a slot of width $e=10^{-3}$ m ($e=0.5\times10^{-2}l$) and length $\lambda=0.379$ m ($\lambda=0.97l_a$), applied close to the separation line, at the top of the rear window [12], by a Dirichlet condition on suction velocity V_{asp} (Figure 2(a)). The direction of the suction velocity is perpendicular to the rear window (Figure 2(b)) at a suction velocity equal to 0.6 times the external flow velocity V_0 [12]. The inlet velocity is maintained at the same intensity as without control to clearly show the control effect. It is known that the suction will affect the pressure field around the body and modify the inlet velocity. In addition, the actuator produces the noise, but it was demonstrated that its level is relatively low [8].

In the following developments, the flow topology is analysed and compared with the topology obtained without control [11] to define the influence of the suction control on the separated flow.

INFLUENCE OF CONTINUOUS SUCTION—FLOW TOPOLOGY

The flow topology analysis is conducted on an iso-surface of total pressure loss ($C_{pi}=1$) and friction line traces without control (Figure 3(a)) and with control (Figure 3(b)). The rear window

DOI: 10.1002/fld

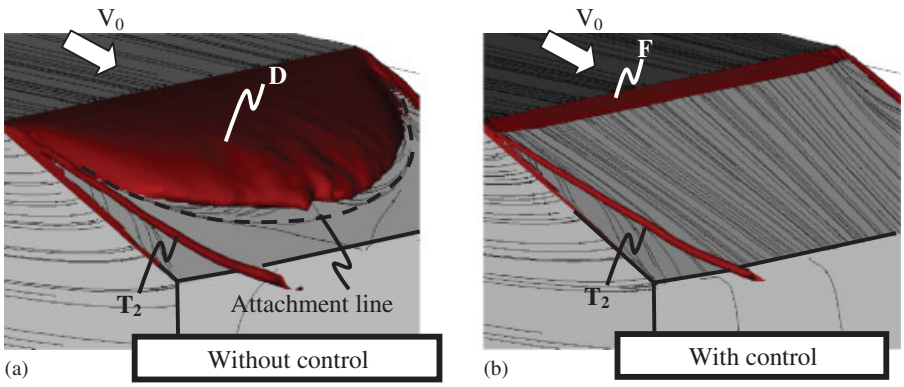

Figure 3. Total pressure loss iso-surfaces ($C_{pi}=1,22$) and friction line traces on rear window: (a) without control and (b) with suction.

separated zone and longitudinal vortices are then analysed according to velocity, static pressure and vorticity fields.

The results in Figure 3(a) and (b) indicate that suction is conducive to eliminating the development of the separated layer D, and to significantly reducing the associated and energy loss. A residual layer, associated with the total pressure loss induced by the suction, remains apparent on the upper part of the rear window (annotated F in Figure 3(b)). However, the separated zone then disappears downstream in the rear window. It is possible to confirm this result by observing the friction lines: when suction is applied (Figure 3(b)), the friction lines remain aligned and in parallel to the direction of the main flow, which indicates that the flow is still attached to the wall on the rear window. The vorticity near the wall, identified under the separated layer without control [17], disappears totally when the suction system is activated (Figure 3(b)).

The results in Figure 3(a) and (b) reveal that suction has the effect of eliminating the rear window separation. Considering the interaction between the longitudinal vortices and the separated zone [17], the structure of the vortices should, however, be analysed more accurately when the suction is applied. Each of the constituent longitudinal and transversal vortices of the wake is then characterized in the following developments according to static pressure, velocity and vorticity fields to analyse the mechanisms of the suction control.

Suction influence on the rear window separated zone

The elimination of the rear window separation is analysed according to the velocity profiles measured in the longitudinal plane (symmetry plane). The coordinate $(x_3 y_3)$ defined in Figure 4 is associated with the separated zone. The datum point of the coordinate is located at the upper edge of the rear window and axis (Ox_3) is tangent to the rear window, in the median longitudinal plane. The velocity profiles in the boundary layer indicated in Figure 4 represent the evolution of the tangential velocity V_{x3} in the direction y_3, for the different coordinates: $x_3/l=0.05$ (Figure 4(a)), $x_3/l=0.5$ (Figure 4(b)) and $x_3/l=0.9$ (Figure 4(c)).

Without control, the negative velocities measured close to the wall (first near wall node: $y_3=2.5\times10^{-4}$ m) on the upper part of the rear window ($V_{x3}=-7.5\times10^{-2}V_0$ at $x_3/l=0.05$, Figure 4(a)) indicate the presence of a backward flow that moves towards the top of the rear window,

DOI: 10.1002/fld

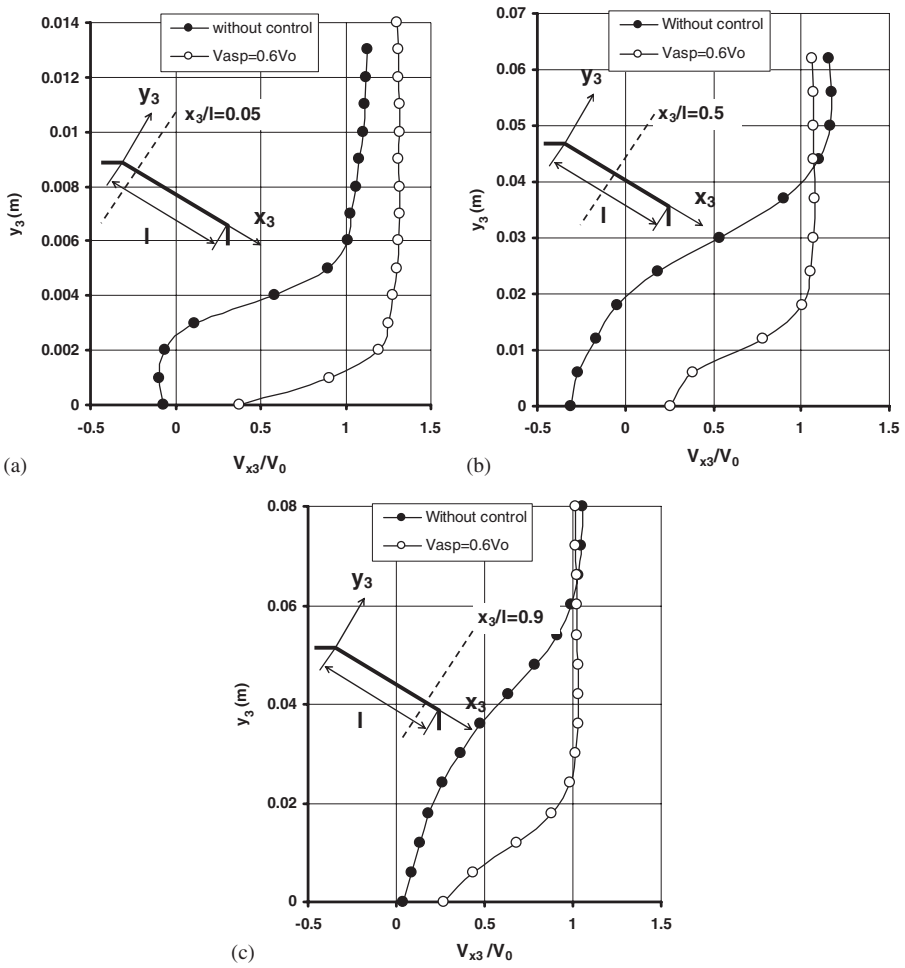

Figure 4. Tangential velocity profiles measured in longitudinal median plane of the rear window, with and without control: (a) at coordinate $x_3/l=0.05$; (b) coordinate $x_3/l=0.5$; and (c) coordinate $x_3/l=0.9$.

under the separated zone [17]. The suction line is conducive to increasing the flow velocity close to the wall. The local velocities become positive ($V_{x3}=37.5\times10^{-2}V_0$ at $x_3/l=0.05$, Figure 4(a)) and the flow remains attached (see Figure 3(b)). Similar results are observed at coordinate $x_3/l=0.5$ (Figure 4(b)). The backward flow is eliminated and the velocities in the vicinity of the wall evolve from $V_{x3}=-32.5\times10^{-2}V_0$ without suction to $V_{x3}=25\times10^{-2}V_0$ ($x_3/l=0.5$, Figure 4(b)) when suction is applied.

Finally, the velocity measurements reveal that the velocity increase at the near wall, when suction is applied, remains significant down to the bottom of the rear window ($x_3/l=0.9$ in Figure 4(c)).

Wall static pressure loss fields are plotted on the rear window (without control Figure 5(a) and with control Figure 5(b)) to complete the analysis. The static pressure distributions measured under the longitudinal vortices, in the vicinity of the lateral edges, are discussed in Section 2 and

DOI: 10.1002/fld

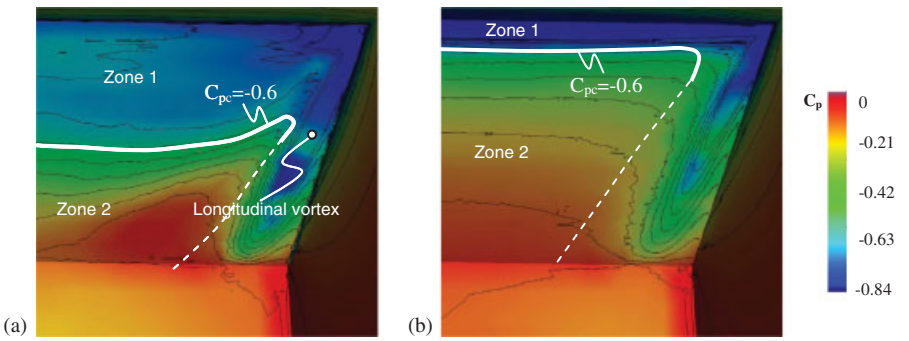

Figure 5. Static pressure loss fields on rear window: (a) without control and (b) with control ($V_{asp} = 0.6V_0$).

the analysis is conducted on two areas (zone 1 and zone 2, Figure 5) delimited by an iso static pressure line corresponding to $C_{pc} = -0.6$.

Without control (Figure 5(a)), the total pressure loss in the separation zone leads to a depression on the wall, with $C_p < -0.6$ (zone 1 in Figure 5(a)), associated with the near wall circulation of the fluid under the separated layer [17] (see Figure 3(a)). The suction first induces a significant local depression on the suction slot (zone 1, Figure 5(b)). This depression is conducive to increase locally the velocity on the top of the rear window, see Figure 5(a), and to remain the streamlines attached on the rear window (Figure 3(b)). The surface of the zone 1 is thereby reduced significantly (Figure 5(b)) and the static pressure then increases regularly in zone 2, along the rear window, whereas the flow slows down ($C_p = -0.1$ at the end of the rear window, with and without control). Overall, the application of suction results in a mean increase to the static pressure on the rear window (zone 2, Figure 5(b)). The depression created on the top of the rear window is compensated by the recompression on the bottom of the rear window. This pressure increase is associated with a reduction in the contribution of the rear window to the pressure drag, which can be estimated as follows:

$$F_{xp} = \frac{\rho V_0^2}{2} \int_{S_c} C_p \mathbf{n} \cdot \mathbf{x} \, \mathrm{d}S \tag{2}$$

where F_{xp} is the pressure drag applied on the surface S_c, $\mathbf{n}$ the normal exiting surface S_c and $\mathbf{x}$ the longitudinal direction of the flow.

On the side parts of the rear window, the static pressure fields in Figure 5(a) and (b) indicate that the static wall pressure increases locally under the longitudinal vortices, a result indicative of a modification occurring on the vortex topology. The influence of suction on the longitudinal vortices is then analysed in the following part.

Suction influence on the longitudinal vortices

Suction has the effect of eliminating the separation zone on the rear window, as shown in Section 1. This structure, however, reacts significantly with the longitudinal vortices [17] and suction may interfere with their development. The structure of vortex T_2 is then analysed with and without suction according to the profiles of velocity, vorticity and static pressure loss coefficient, measured in a vortex cross section located at coordinate $x_2/l = 0.5$, i.e. downstream from the vortex formation

DOI: 10.1002/fld

area identified without control [17]. Coordinate $(Ox_2y_2z_2)$ is associated with the vortex axis (see Figure 6), which defines angles β with respect to the longitudinal direction x and θ with respect to the surface of the rear window (see Figure 6). Computation of angles θ and β with and without suction indicates that this has no significant impact on the position of the vortex axis.

Azimuthal velocity profiles. The azimuthal velocity profiles $V_{z2}(y_2, z_2 = 0)$ in Figure 7(a) indicate that suction does not has a significant influence on the topology of the longitudinal structures; the velocity profiles obtained with and without control are similar. The results, however, highlight an increase in distance L measured between the azimuthal velocity extreme, once suction is applied

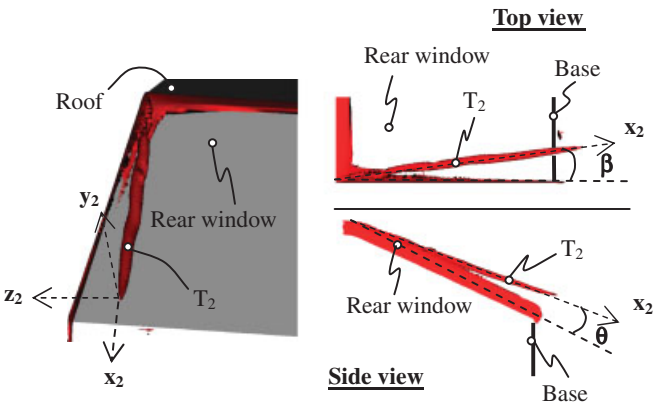

Figure 6. Definition of coordinate system associated with longitudinal left-hand vortex T_2 (vorticity iso-contour surface $(\omega = 10^4\,\mathrm{s}^{-1})$).

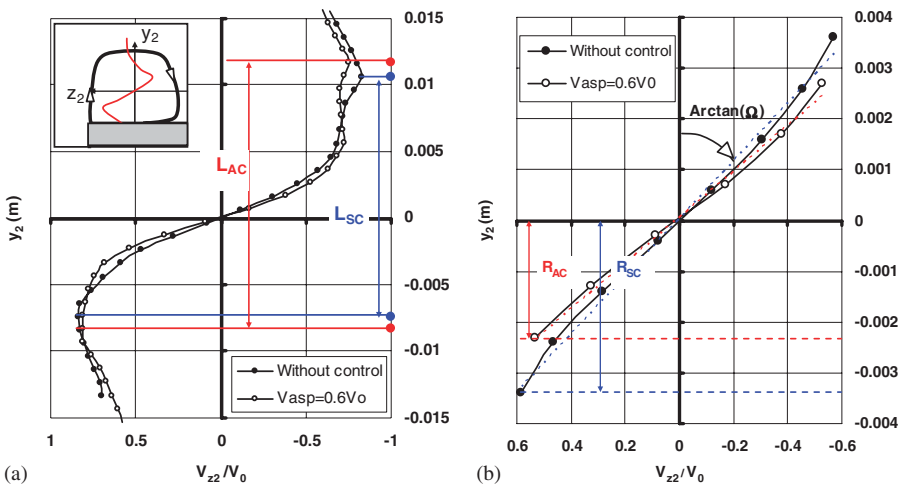

Figure 7. Azimuthal velocity profiles in the vertical direction, measured in transverse plane located coordinate $x_2/l = 0.5$: (a) in the longitudinal structure T_2 and (b) in the vortex core.

DOI: 10.1002/fld

($L_{AC} > L_{SC}$ in Figure 7(a)). Hence, the suction line applied on the top of the rear window induces a spreading of the longitudinal vortex structure in the transverse direction. This spreading is associated with an increase in vorticity at the vortex centre, $\omega_x = 14 \times 10^3\,\mathrm{s}^{-1}$ without control as opposed to $\omega_x = 17.5 \times 10^3\,\mathrm{s}^{-1}$ with control, which promotes the dissipation of the jet [23]. At the vortex core defined by the linear evolution of the azimuthal velocity (Figure 7(b)), the increase in vorticity is highlighted by means of the azimuthal velocity gradient (gradient Ω defined in Figure 7(b)), which characterizes a local rotation of the fluid. Gradient Ω increases when suction is applied: $\Omega = 9125\,\mathrm{s}^{-1}$ with control vs $\Omega = 7120\,\mathrm{s}^{-1}$ without control. If suction promotes the dissipation of the jet (Figure 7(a)), the vortex core on the other hand is inclined to become narrower: the viscous radius R, defined as the distance at which the evolution of the azimuthal velocity is linear, decreases when the suction system is activated ($R_{AC} < R_{SC}$, Figure 7(b)).

It is, therefore, difficult to draw a conclusion at this point with respect to the influence of suction on the contribution of the longitudinal structures to aerodynamic drag. Whereas suction causes an increase to the transverse section of the structures (Figure 7(a)) and an increase of vorticity in the vortex core (Figure 7(b)), the viscous radius at which vorticity is maximum is reduced. The results presented in this paragraph must, therefore, be completed by axial velocity and static pressure profiles measured in the vortex.

Axial velocity and static pressure loss profiles. The axial velocity is measured in the vortex core at coordinate $x_2/l = 0.5$, with and without control, and the results are indicated in Figure 8(a). The axial velocity profiles (Figure 8(a)) are not modified significantly when suction is applied. The profiles obtained without control and with control exhibit a jet-type structure, with a velocity V_x greater than reference velocity V_0 at the centre of the vortex. The results indicate, however, a shift on the axial velocity troughs on either side of the vortex core, which move away from the vortex axis when suction is applied (Figure 8(a)). This phase shift is associated with an increase of distance L between the azimuthal velocity extremes highlighted in Figure 7(a). Finally, the static pressure loss coefficient profiles (Figure 8(b)) indicate that the static pressure losses are more

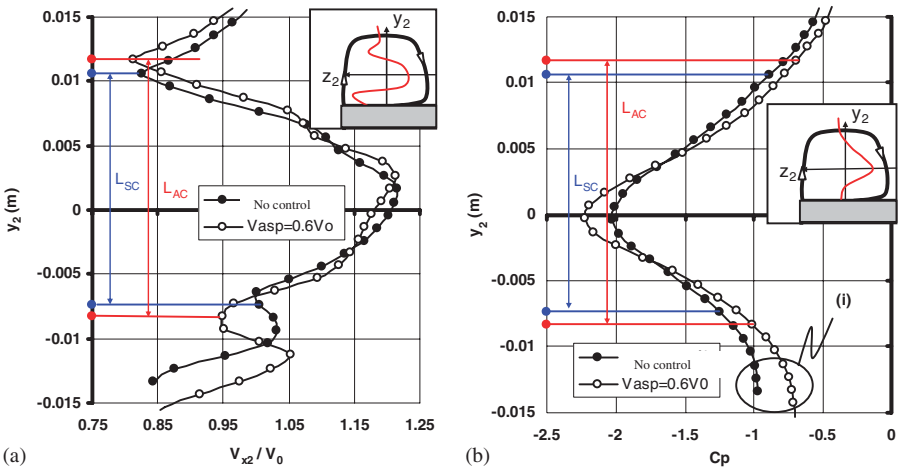

Figure 8. Velocity and static pressure profiles in the vertical direction, measured in vortex T_2, cross-section plane at coordinate $x_2/l = 0.5$: (a) axial velocity and (b) static pressure loss coefficient.

DOI: 10.1002/fld

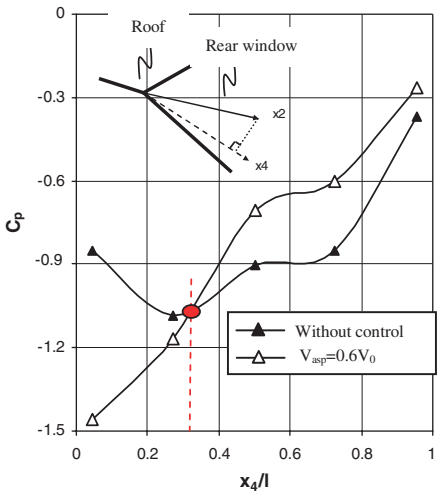

Figure 9. Static pressure loss coefficient measured along the projection of the vortex axis on the wall.

significant in the vortex core when suction is applied: $C_p=-2$ at centre ($y_2=0$) without control vs $C_p=-2.2$ with suction. Conventionally, this result is associated with an increase of the vorticity at the vortex core, highlighted in Figure 7(b). On the other hand, as the distance from the core of the vortex increases at $y_2>0.005$ or $y_2<-0.005$, the effect is reversed and the static pressure measured without control is less than the static pressure measured with suction (Figure 8(b)). Hence, close to the wall ($y_2<-0.013$), the static pressure loss coefficient switches from $Cp=-0.98$ without control to $Cp=-0.72$ with suction ((i) Figure 8(b)). This result highlights an increase in static pressure under the vortex, at the location of the wall, already observed in Figure 5(b), associated with the reduction of the viscous radius R (Figure 7(b)).

The influence of the vortex on the rear window, with and without suction, is analysed according to the static pressure loss measured along the projection of the vortex axis on the wall (axis x_4 defined in Figure 9). Rotation of the fluid in the longitudinal vortex induces a depression on the wall as highlighted in Figure 5(a) and (b). Without control, the static pressure is decreasing for $x_4/l<0.25$ ($C_p=-0.85$ for $x_4/l=0.05$ and $C_p=-1.1$ for $x_4/l=0.25$, Figure 9). This decrease is associated with an increase in vorticity in the shear layer [11]. At $x_4/l>0.3$, the structure of the vortex is well-established [11] and the vortex axis moves away from the wall, its influence on the wall diminishes and the wall pressure increases ($C_p=-0.35$ for $x_4/l=0.95$).

The presence of suction leads to an additional depression on the top of the rear window ($C_p=-1.5$). This depression is associated with an increase of vorticity in the vortex when suction is applied, already mentioned in the previous paragraph. The evolution of the static pressure loss coefficient then increases in the direction x_4, over the whole length of the rear window, which suggests that the structure of the vortex becomes established higher up on the rear window when suction is applied. The static pressure measured with suction is, therefore, more significant with suction, for $x_4/l>0.3$. This recompression observed under the vortex (Figures 5(b), 8(b) and 9) is associated with the reduction of the transverse development at the vortex core, as mentioned in the previous paragraph (Figure 7(b)), and is conducive to reducing the contribution of the longitudinal structures towards the drag pressure, according to Equation (4).

DOI: 10.1002/fld

To sum up, suction has the effect of increasing the fluid rotation in the vortex core (Figure 7(a)) and the associated volume energy loss as a result. According to the Onorato equation (second and third term of Equation (2)), suction is inclined to increase the contribution of the longitudinal vortices into aerodynamic drag. However, the analysis also highlights an increase in the static wall pressure under the vortex axis (Figures 5(b), 8(b) and 9), associated with the reduction in the viscous radius of the vortex (Figure 7(b)), which prompts a reduction of the pressure drag and may compensate for the volume pressure losses.

Suction influence on the near-wake flow

The near-wake flow topology is analysed on total pressure loss and streamlines fields measured in the longitudinal median plane, without control (Figure 10(a)) and with control (Figure 10(b)).

The streamlines emanating from the roof roll up in the separation zone around a vortex centre C_3 (Figure 10(a) and (b)) and a singular source point (F, Figure 10(b)), highlighted at the lower part of the rear window, reveal a saddle point S_2 (Figure 10(a) and (b)). The streamlines emanating from the rear window and underbody then roll around at the base into two counter-rotating transverse vortices of centre C_1 and C_2 (Figure 10(a)). The rotation of these two swirling structures reveals a saddle point S_1, located at $x/h_c = 0.88$ downstream from the base (with h_c the base height, Figure 10(a)), which indicates the end of the recirculation zone. Finally, the attachment point N is located at the bottom of the base, at coordinate $y_N/h_c = -0.37$. The lower vortex (with centre

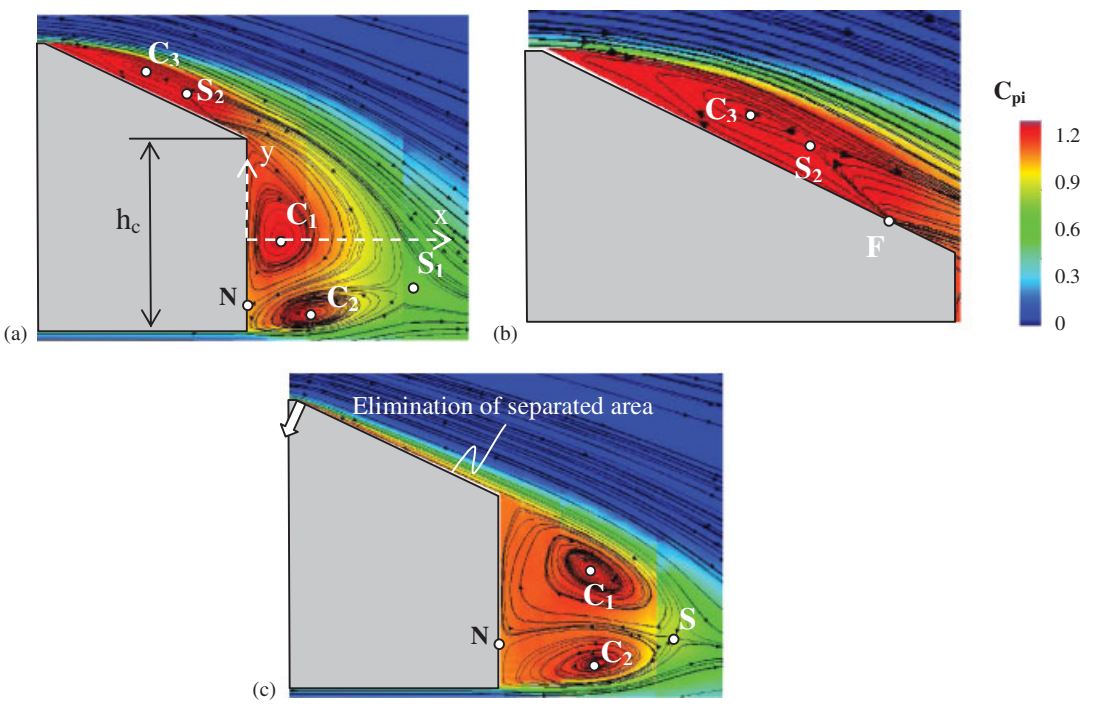

Figure 10. Total pressure loss coefficient fields, measured in the longitudinal median plane: (a) without control; (b) without control on rear window; and (c) with control.

DOI: 10.1002/fld

C_2 at bottom of base, Figure 10(a)) is less developed, as a result of the velocity deficit in the underbody, as indicated by Chometon and Gilliéron [29].

When suction is applied (Figure 10(c)), the separated zone of the rear window disappears and the streamlines remain in parallel to the rear window. These results have already been mentioned in the previous paragraphs. The velocity increase on the rear window, highlighted in Figure 4, is reflected by an increase of vorticity in the structure of vortex centre C_1. The interaction between these two vortices and the wall then causes a displacement of the vortex centres and of the attachment point (Figure 10(c)). The position of vortex centres C_1 and C_2, and of attachment point N, with and without control, is given in Table I.

The results indicate that vortex centres C_1 and C_2 move downstream when the suction system is activated, and that they become aligned on the same abscissa $x/h_c=0.48$. The structure of vortex centre C_1 remains, however, more significant and the attachment point N is situated on the bottom of the base. The relative position of vortex centres in the vertical direction is inclined, however, to become more consistent around the median position $y/h_c=0$, whereas attachment point N rises on the base. The results in Table I and Figure 10 suggest, therefore, that suction is conducive to balancing the symmetry of the near-wake flow.

The previous results are complemented in Figure 11 by a total pressure loss profile measured in the longitudinal plane at coordinate $x/h_c=0.25$ downstream from the base. The datum point of the vertical axis is fixed at the centre of the base, in accordance with Figure 10. The results

Table I. Positions of points C_1, C_2 and N, with and without control.

	X_{C1}/h_c	X_{C2}/h_c	Y_{C1}/h_c	Y_{C2}/h_c	Y_N/h_c
Without control	0.17	0.32	0	−0.38	−0.34
With control	0.47	0.49	0.17	−0.34	−0.23

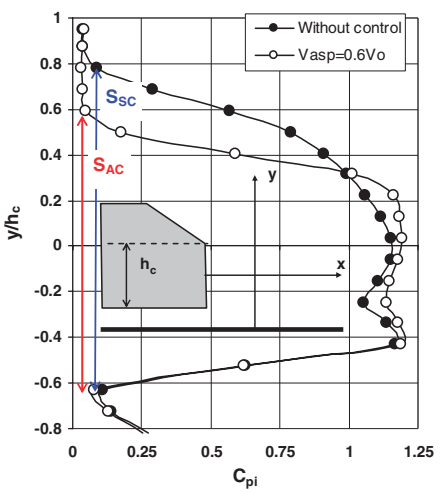

Figure 11. Transverse distribution of total pressure loss coefficient measured in longitudinal median plane at $x/h_c=0.25$.

DOI: 10.1002/fld

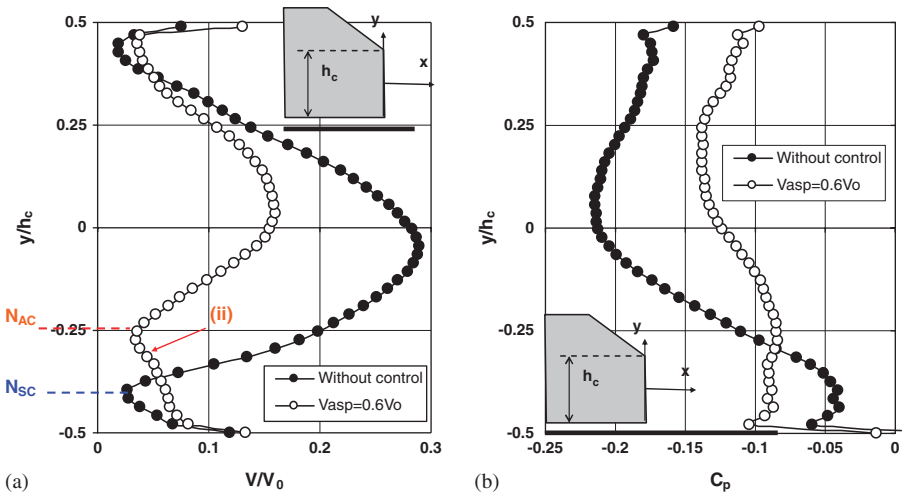

Figure 12. Transverse velocity and static pressure distributions measured on base ($x/h_c=0.005$) without control and with control: (a) velocity distribution and (b) static pressure loss coefficient distribution.

reveal a reduction of the wake cross section, already identified on a 2D configuration [12]. The transverse development of the wake is, therefore, arbitrarily characterized by length S at which the total pressure loss coefficient is greater than 0.1 (see Figure 12). This criterion is used to determine the transverse wake sections without control ($S_{SC}=1.41h_c$) and with control ($S_{AC}=1.22h_c$).

At $-0.4<y/h_c<0.3$, the elimination of the rear window separated zone does not significantly modify the total pressure loss and the total pressure loss coefficient ($C_{pi}=1.1$) remains quasi-uniform, with or without control. The quasi-uniformity of the total pressure (for $-0.4<y/h_c<0.3$), therefore, leads to

$$P_{SC}+\rho\frac{V_{SC}^2}{2}=P_{AC}+\rho\frac{V_{AC}^2}{2}=C^{\text{ste}} \tag{3}$$

in which P_{SC} and P_{AC} are the static pressure measured without control and with control, respectively, and V_{SC} and V_{AC} the respective velocities.

The velocity and static pressure profiles, obtained in the longitudinal median plane on the base surface (at coordinate $x/h_c=0.005$), are given in Figure 12(a) and (b), respectively.

The results reveal a velocity maximum, observed close to the base centre without control ($V=0.29V_0$ at $y/h_c=-0.05$, Figure 12(a)) or with control ($V=0.15V_0$ at $y/h_c=0.03$, Figure 12(a)), which corresponds to the presence of the upper swirling structure (of centre C_1, see Figure 10(a) and (b)). The velocity then decreases closer to the upper or lower edges of the base (at $y/h_c=0.5$ and $y/h_c=-0.5$, respectively), due to the presence of a separation point on the top of the base, and of the attachment point N on the bottom of the base (N_{SC} without control, N_{AC} with control, see Figure 12(a)). As the suction is applied, a velocity plateau ((ii) in Figure 12(a), with $V=0.05V_0$) appears close to the attachment point N_{AC}, which corresponds to the structure of centre C_2, having a lower energy level. This plateau does not appear without control since attachment point N_{SC} is located at the bottom of the base.

DOI: 10.1002/fld

Overall, suction is reflected by a velocity reduction in the near wake, which leads to an increase of the static pressure on the base wall, according to Equation (5) (Figure 12(b)). At $y/h_c > -0.3$, the static pressure distribution obtained with control is homogenous over the whole height of the base, with $C_{\text{pmoy}} = -0.11$ vs $C_{\text{pmoy}} = -0.15$ without control (Figure 12(b)).

The overall effect of suction on aerodynamic drag is analysed in the following development to quantify the performance of the control. Several suction velocities are tested in order to optimize the ratio between the energy saved by reducing the aerodynamic drag and the energy consumed to generate the suction flux.

INFLUENCE OF CONTINUOUS SUCTION—AERODYNAMIC PERFORMANCES

The suction influence is analysed according to the aerodynamic forces applied to the geometry, with and without control, and the results are presented through aerodynamic drag reduction with respect to the reference configuration (without control).

The mean drag coefficients, obtained at different suction velocities, are indicated in Figure 13, and the drag reductions obtained with respect to the reference configuration (without control) are also indicated. The results reveal two variation phases of the aerodynamic drag as a function of the suction velocity, which highlight a singular suction velocity, $V_{\text{asp}} = 0.6V_0$, already identified in the 2D configuration [12].

In the first phase (phase 1 in Figure 13), the control performance increases very rapidly with the suction velocity. The reductions obtained are 12.7% for $V_{\text{asp}} = 0.375V_0$ and 17.2% for $V_{\text{asp}} = 0.6V_0$. These results suggest significant modifications in the flow topology for $V_{\text{asp}} < 0.6V_0$. Figure 14, therefore, represents a total pressure loss iso-surface ($C_{pi} = 1.22$) obtained at $V_{\text{asp}} = 0.375V_0$, completed by the friction lines field. The results suggest that the control mechanisms applied in this case are different from those found in the literature on the suctioned wake control of a

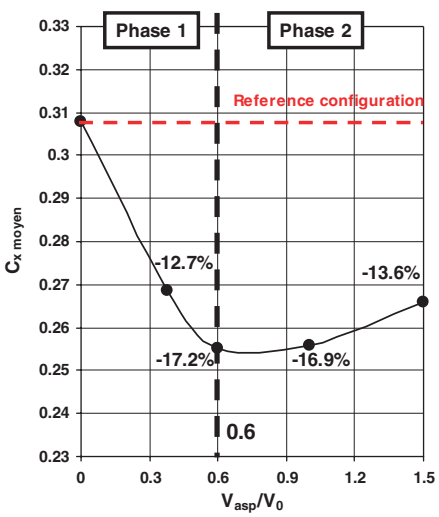

Figure 13. Evolution of the time-averaged drag coefficient as a function of suction velocity.

DOI: 10.1002/fld

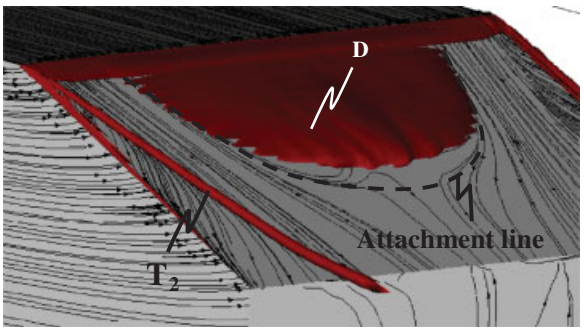

Figure 14. Total pressure loss iso-surface ($C_{pi}=1.22$) and friction lines fields on rear window, with $V_{\text{asp}}=0.375V_0$.

cylinder [10, 11]. Whereas the suction moves the fluid separation line downstream, in the case of the cylinders, it is inclined to limit the development of the separated area by raising the attachment line of the fluid on the rear window in the direction of the suction line (Figure 14). The separation line is indeed fixed by the gradient declivity between the roof and the rear window and cannot be pushed downstream in the present configuration. The results indicated in Figure 14 reveal that the application of suction, at $V_{\text{asp}}=0.375V_0$, prompts the re-attachment of the flow to the middle of the rear window; the volume of the separated area is, therefore, reduced with respect to the reference configuration indicated in Figure 3(a), which explains the drag reduction observed in Figure 13 (-12.7%). The topology of the airflow then varies rapidly with the suction velocity, as long as the separated area of the rear window is not totally eliminated, at $V_{\text{asp}}=0.6V_0$.

Conversely, during the second phase (phase 2 Figure 13), the drag is inclined to increase; the reductions obtained are 17.2% for $V_{\text{asp}}=0.6V_0$ and 13.6% for $V_{\text{asp}}=1.5V_0$. The flow is totally attached to the rear window at $V_{\text{asp}}=0.6V_0$ (Figure 3(b)). An increase in suction velocity, therefore, only prompts an increase of static wall pressure loss on and close to the slot, which leads to an increase of the pressure drag (Equation (4)). Likewise, the total pressure loss associated with the vorticity created locally at the slot increase with the suction velocity and contribute towards energy losses, which increase the aerodynamic drag value.

The drag reductions presented in Figure 13 indicate that there is an optimum velocity in terms of drag reduction ($V_{\text{asp}}=0.6V_0$), and the results are similar to those observed in 2D [12]. When developing active flow control solutions that use an external energy source, it is, however, necessary to ensure that the system runs efficiently, i.e. that the energy used to generate the control is less than the energy saved through aerodynamic drag reduction. Efficiency η of the solution is thus evaluated according to

$$\begin{aligned} \eta &= \frac{P_{ec}}{P_c} \\ P_{ec} &= \Delta F_x V_0 \\ P_c &= K\frac{\rho V_{\text{asp}}^3 S_{\text{asp}}}{2} \end{aligned} \tag{4}$$

where P_{ec} and P_c represent the energy saved through aerodynamic drag reduction and the energy used to generate the control, respectively, K represents a generic total pressure loss [30]. S_{asp} is the suction surface and ΔF_x is the drag reduction induced by the suction. The control is considered efficient

DOI: 10.1002/fld

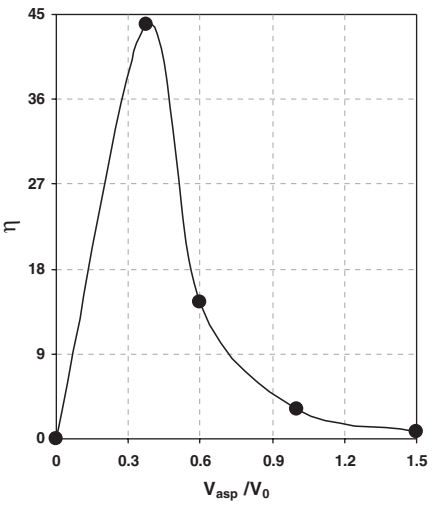

Figure 15. Control efficiency η as a function of suction velocity.

when the value η is equal to or greater than $\eta_c = 1$. Here, the consumed energy is due to the total pressure loss generated through the suction slot (K_{slot}) and to the losses occurring in the upstream circuit (K_{sys}). Usually, during continuous flow through a given orifice, K_{slot} is set to 1.5 to take into account the inlet and outlet effects of the slot [31]. Inside the pumping system, the pressure loss K_{sys} is arbitrarily set to 3.5. The total pressure loss coefficient K of the total system is thus equal to 5.

The results given in Figure 15 reveal that the control efficiency is maximum at $V_{\text{asp}} = 0.375 V_0$. The power saved is, therefore, 41 times greater than the power consumed. The efficiency then decreases rapidly at higher suction velocities; however, they remain greater than $\eta_c = 1$. The control, therefore, remains efficient in this velocity range. It is of interest to note that the efficiency is maximum at a velocity corresponding to phase 1 identified in Figure 13, i.e. a suction velocity at which the separated zone on the rear window is not totally eliminated.

The critical efficiency $\eta_c = 1$ is used to determine a critical coefficient K_c beyond which control is no longer economically viable

$$K_c = 2\frac{\Delta F_x V_0}{\eta_c \rho V_{\text{asp}}^3 S_{\text{asp}}} \tag{5}$$

This critical coefficient characterizes the maximum total pressure losses acceptable at which the suction system remains efficient. At a suction velocity $V_{\text{asp}} = 0.375 V_0$, the critical total pressure loss coefficient is $K_c = 205$. This result, therefore, highlights the potential of a suction system operating at a very low flow rate, and the possibility of envisaging a high total pressure loss, while remaining efficient.

CONCLUSION AND PERSPECTIVE

An active flow control solution by continuous suction is tested to reduce the aerodynamic drag on a simplified fastback geometry. The continuous suction is set up according to a preliminary

DOI: 10.1002/fld

2D numerical study and the analysis of the flow topology with and without control is carried out according to the 3D numerical lattice Boltzmann method. The suction influence on each of the vortices interacting in the near-wake flow is studied and the drag reductions obtained are discussed.

Suction is conducive to creating significant local depression on the separation line identified without control, which has the effect of re-attaching the flow on the wall. A parametric analysis indicates that the re-attachment occurs at a suction velocity of $24\,\mathrm{m\,s^{-1}}$ (corresponding to $0.6V_0$). The elimination of the rear windows separated zone, therefore, prompts a reduction of the total pressure loss in the wake, a reduction in the wake cross section and an increase of the wall static pressure on the rear part of the geometry (rear window and base). The drag reductions associated with these modifications are close to 17% and the suction velocity increase, at $V_{\mathrm{asp}}>0.6V_0$, does not improve such a reduction significantly. Likewise, the drag reductions rapidly decrease when the suction velocity diminishes below $0.6V_0$. Considering the power consumed to generate suction, the suction velocity that maximizes the efficiency of control is, however, $0.375V_0$. At this velocity, the suction remains efficient with significant total pressure loss on the slot.

This study also analyses the influence of suction on the longitudinal vortices, which significantly interact with the rear window separated zone. The vorticity and total pressure loss associated with the longitudinal vortex core increases as the suction is applied. This increase is reflected by a reduction of the viscous radius in the vortex core, which prompts a wall static pressure increase under the vortex axis, on the rear window. Suction, however, does not significantly modify the structure of the vortices.

The importance of the energy losses in the longitudinal swirling structures indicates the necessity of specific control systems, conducive to limiting their contribution towards the development of aerodynamic drag. The use of two suction slots located on the side edge of the rear window constitutes an interesting perspective capable of reducing, even eliminating, the development of these structures. The combined use of these two configurations could prompt significant aerodynamic drag reductions. Another solution would consist in placing blowing sections on the side edges in order to increase the vorticity of the vortices and provoke their breakdown [25]. Finally, blowing solutions may be envisaged in order to move the transverse vortices highlighted on the periphery of the base downwards. The objective is, therefore, to limit the static pressure losses by reducing the velocity distribution on the base.

These solutions are currently being analysed and offer a notable potential for reducing aerodynamic drag and automobile fuel consumption. The results presented in this paper confirm the potential of active suction control in the automobile industry. The results should, however, be corroborated by experimental results and tested on real car flow configuration.

REFERENCES

1. Hucho WH. Aerodynamics of road vehicle. *Annual Review of Fluid Mechanics* 1998; **25**:485–537.
2. Gad-El-Hak M. Modern developments in flow control. *Applied Mechanics Reviews* 1996; **9**:365–379.
3. Gad-El-Hak M, Pollard A, Bonnet J (eds). *Flow Control*: *Fundamentals and Practices*. Springer: Berlin, 1998.
4. Collis SS, Joslin RD, Seifert A, Theofilis V. Issues in active flow control: theory, control, simulation, and experiment. *Progress in Aerospace Sciences* 2004; **40**:237–289.
5. Bewley T, Liu S. Optimal and robust control and estimation of linear paths to transition. *Journal of Fluid Mechanics* 1998; **365**:305–349.
6. Cathalifaud P, Luchini P. Optimal control by blowing and suction at the wall of algebraically growing boundary layer disturbances. In *Proceedings of the IUTAM Laminar-turbulent Symposium*, V. Sedona, AZ, U.S.A., Saric W, Fasel H (eds). 2002; 307–312.

DOI: 10.1002/fld

7. Glezer A, Amitay M. Synthetic jets. *Annual Review of Fluid Mechanics* 2002; **34**:503–529.
8. Kourta A, Vitale E. Analysis and control of cavity flow. *Physics of Fluids* 2008; **20**:077104.
9. Gilliéron P. Contrôle des écoulements appliqués à l'automobile. Etat de l'art. *Mécanique and Industries* 2002; **3**:515–524.
10. Bourgois S, Tensi J. Contrôle de l'écoulement par autour d'un cylindre par techniques fluidiques et acoustiques. *16eme Congrès Français de Mécanique*, Nice, 2003.
11. Fournier G, Bourgois S, Pellerin S, Ta Phuoc L, Tensi J, El Jabi R. Wall suction influence on the flow around a cylinder in laminar wake configuration by large eddy simulation and experimental approaches. *39e Colloque d'Aérodynamique Appliquée*, *Contrôle des écoulements*, Mars, Paris, 2004; 22–24.
12. Rouméas M, Gilliéron P, Kourta A. Réduction de traînée par contrôle des décollements autour d'une géométrie simplifiée: etude paramétrique 2D. *17ème Congrès Français de Mécanique*, *29 Août au 02 Septembre* 2005, Troyes, 2005.
13. Onorato M, Costelli AF, Garonne A. Drag measurement through wake analysis. *SAE*, *SP-569*, *International Congress and Exposition*, Detroit, 1984.
14. Ahmed SR, Ramm R, Falting G. Some salient features of the time averaged ground vehicle wake. *SAE Technical Paper Series 840300*, Detroit, 1984.
15. Spohn A, Gilliéron P. Flow separations generated by a simplified geometry of an automotive vehicle. *Congrès IUTAM Symposium on Unsteady Separated Flows*, 8–12 April 2002, Toulouse, France, 2002.
16. Beaudoin JF, Cadot O, Aider JL, Gosse K, Paranthoën P, Hamelin B. Cavitation as a complementary tool for automotive aerodynamics. *Experiments in Fluids* 2004; **37**:763–768.
17. Rouméas M, Gilliéron P, Kourta A. Separated flows around the rear window of a simplified car geometry. *Journal of Fluids Engineering* 2008; **130**:021101-1.
18. Rouméas M. Contribution à l'analyse et au contrôle du sillage épais par aspiration ou soufflage continu. *Ph.D. Thesis*, *Thèse de Doctorat*, INP Toulouse, 2006.
19. Rouméas M, Gilliéron P, Kourta A. Analysis and control of the near–wake flow over a square-back geometry. *Computers and Fluids* 2008; DOI: 10.1016/j.compfluid.2008.01.009.
20. Chen S, Chen H, Martinez D, Matthaeus W. Lattice Boltzmann model for simulation of magnetohydrodynamics. *Physical Review Letters* 1991; **67**:3776–3779.
21. Chen S, Chen H, Matthaeus W. Recovery of the Navier–Stokes equations using a lattice-gas Boltzmann method. *Physical Review A* 1992; **45**:R5339–R5342.
22. Bhatnagar PL, Gross EP, Krook M. A model for collision processes in gases. Small amplitude processes in charged and neutral one-component systems. *Physical Review* 1954; **94**(3):511–525.
23. Chen H, Teixeira C, Molvig K. Digital physics approach to computational fluid dynamics: some basic theoretical features. *International Journal of Modern Physics C* 1997; **8**(4):675–684.
24. Yakhot V, Orszag SA. Renormalization group analysis of turbulence. Basic theory. *International Journal of Scientific Computing* 1986; **1**:1–51.
25. Pervaiz M, Teixeira M. Two equation turbulence modeling with the lattice-Boltzmann method. *Proceedings of ASME PVP Division Conference*, *Second International Symposium on Computational Technologies for Fluid/Thermal and Chemical Systems with Industrial Applications*, Boston, 1999.
26. Gilliéron P, Chometon F. Modelling of stationary three-dimensional detached airflows around an Ahmed reference body. *Third International Workshop on Vortex*, *ESAIM*, *Proceedings*, vol. 7, 1999; 173–182. Available from: http://www.emath.fr/proc/Vol7/.
27. Krajnovic S, Davidson L. Flow around a simplified car, part 1: large eddy simulation. *Journal of Fluids Engineering* 2005; **127**:907–918.
28. Krajnovic S, Davidson L. Flow around a simplified car, part 2: understanding the flow. *Journal of Fluids Engineering* 2005; **127**:919–928.
29. Chometon F, Gilliéron P. Modélisation des écoulements tridimensionnels décollés autour des véhicule automobiles. *Revue Ingénieurs de l'automobile* (*SIA*), *Aérodynamique*, *Aéroacoustique & Aérothermodynamique Automobile et Ferroviaire* 1997; **711**:50–56. ISSN 0020-1200.
30. Lehugeur B, Gilliéron P, Ivanic T. Contribution de l'éclatement tourbillonnaire à la réduction de la traînée des véhicules automobiles: approche numérique. *Comptes Rendus Mécanique* 2006; **334**:368–372.
31. Idel'Cik IE (ed.). *Memento des Pertes de Charges*. Eyrolles: Paris, 1986.

DOI: 10.1002/fld